Available online at www.sciencedirect.com
SCIENCE DIRECT®
Journal of Solid State Chemistry 175 (2003) 289–298
JOURNAL OF SOLID STATE CHEMISTRY
http://elsevier.com/locate/jssc

EXAFS study of ceria–lanthana-based TWC promoters prepared by sol–gel routes

Francesca Deganello,[a] Alessandro Longo,[a] and Antonino Martorana[b,*]

[a] *ISMN-CNR, via Ugo La Malfa, 153, Palermo I-90146, Italy*

[b] *Dipartimento di Chimica, Inorganica e Analitica "Stanislao Cannizzaro", Università di Palermo, Viale delle Scienze, Palermo I-90128, Italy*

Received 18 December 2002; received in revised form 15 April 2003; accepted 12 May 2003

Abstract

Extended X-ray absorption fine structure (EXAFS) experiments at the Ce K- and La K-edges were performed on ceria–lanthana–alumina three-way catalysts promoters prepared by sol–gel routes, in order to investigate the effect of lanthanum doping on the ceria structure. The formation of $Ce_{1-x}La_xO_{2-x/2}$ solid solution, already observed by X-ray diffraction, was confirmed by EXAFS analysis, while no experimental evidence of a Ce–Al interaction was found. In presence of cerium and aluminum, lanthanum is involved in the formation of solid solution with CeO_2 and of La–Al compounds. When the La:Al molar ratio is sufficiently high, the growth of a tridimensionally ordered $LaAlO_3$ perovskite compound is observed. For increasing values of $x/1-x$ in the solid solution $Ce_{1-x}La_xO_{2-x/2}$, the Ce–O distance decreases, while La–O distance remains nearly constant.

Keywords: Lanthanum-doped ceria; EXAFS; Solid solutions; Oxygen storage capacity; Alumina stabilization; Lanthanum aluminate

1. Introduction

The abatement of pollutants to non-toxic products in automobile exhausts is performed by the so-called three-way catalysts (TWCs) that, in most of the present-day formulations, are constituted of ceria-based compounds [1,2] in synergic cooperation with a precious metal and supported on transition aluminas (usually, γ-alumina).

As well known, the most peculiar property of ceria is its ability of acting as an oxygen buffer with respect to the reaction environment. This property, usually called oxygen storage capacity (OSC), depends on the mobility of oxygen in the ceria network and can be greatly enhanced by suitable modification of the host lattice with various dopants. When the doping is performed using trivalent species, in particular lanthanum [3,4], the improvement of oxygen mobility is due to the anion vacancies that are formed to fulfill the condition of lattice charge neutrality.

A drawback of the use of transition aluminas as support for TWC systems can be the big surface area reduction taking place during the transformation to α-alumina (corundum) between 800°C and 900°C. As these temperatures are easily reached and even exceeded in operating conditions by the catalytic converters, γ-alumina is stabilized against thermal deactivation by different methods such as addition of barium [5], zirconium [6], or rare-earth compounds [7]. In particular, it has been demonstrated that lanthanum improves the thermal stability of γ-alumina [8–10], although its exact role is still under debate. To this concern, two interpretations meet a general agreement: according to the most widely accepted hypothesis, lanthanum forms compounds ($LaAlO_3$ [11], $La_2O_3 \cdot 11Al_2O_3$ [12], La_2O_3 [13]), which coat the alumina surface and hinder the diffusion processes that lead to the formation of the α-phase; alternatively, it was also proposed [14,15] that lanthanum is incorporated in γ-Al_2O_3, producing a stabilization of the structure up to 1100°C.

In a previous paper [16] we reported the synthesis of several Ce–La–Al compounds by two different sol–gel routes, involving the introduction of all the components in a single step. A careful phase analysis, carried out by Rietveld refinements of the X-ray diffraction (XRD) patterns, proved that lanthanum formed a substitutional solid solution in ceria and that, in agreement with the behavior of anionic conductivity

*Corresponding author. Fax: +39-091-427584.
E-mail address: cric2@unipa.it (A. Martorana).

0022-4596/03/$ - see front matter © 2003 Elsevier Inc. All rights reserved.
doi:10.1016/S0022-4596(03)00284-6

in trivalent rare-earth-doped ceria, the best OSC was reached in correspondence of a well-defined composition of the solid solution. Moreover, it was possible to demonstrate by XRD that lanthanum interacts also with aluminum, giving rise in some of the investigated samples to a perovskite $LaAlO_3$ phase. In other cases no direct evidence of a La–Al compound could be achieved. However, taking into account that in all Al-containing samples the overall La amount that could be determined by XRD was less than the input one, it was hypothesized that a noteworthy fraction of La could be dispersed in the alumina matrix.

X-ray absorption spectroscopy (XAS) has been already used for the structural characterization of ceria-based TWC [17] systems, of pure CeO_2 [18–20], of lanthanide-[21,22] or Zr-doped CeO_2 [23,24]. There is only one XAS study on La-doped ceria concerning the X-ray absorption near-edge structure at Ce- and La L_{III}-edges [25]. Extended X-ray absorption fine structure (EXAFS) investigations on La-doped CeO_2 at the L_{III}-edge present some difficulties due to the superposition of the La L_{III}-edge over the Ce L_{III}-edge; also the close proximity of the La L_{II}-edge to the La L_{III}-edge constitutes a problem, since it truncates the useful range over which data can be collected, as it is underlined by an EXAFS study on lanthanum oxide [26]. On the other hand, due to the high photon energies required, the K-edge has been rarely employed in studies on ceria-based compounds, although some investigations are now emerging [27]. To the best of our knowledge, only one EXAFS study [22] exists regarding the local structure of La-doped ceria at the La K- and Ce K-edges, that is focused on the relationships between ionic conductivity and local order around host and dopant cations with different ionic radius. However, although the cited paper deals with different kind of dopants or doubly doped ceria compounds, it does not take into account the effect of different dopant concentrations on the local order around Ce and La. The interactions between lanthanum and alumina have been already studied by different techniques such as NMR and FT-IR [28], EPR [29], XPS [30], and computer simulation [31], but only one XAS study on lanthanide oxides supported on γ-alumina exists [32], showing that the strong interaction between the carrier and the supported phase modifies the white line intensity at the lanthanide X-ray absorption edge.

This paper reports the structural study carried out by EXAFS analysis on the ceria–lanthana–alumina samples previously investigated by XRD [16]. In particular, this EXAFS study has been carried out to get information about the interaction of lanthanum with alumina that could be only partially investigated by XRD, and about the La–O and Ce–O interactions in the fluorite ceria–lanthana phase. Taking advantage of the high energies available at the European Synchrotron Radiation Facility (ESRF) in Grenoble (France), all the EXAFS experiments have been performed at the Ce- and La K-edges.

2. Experimental

2.1. Materials

The sol–gel preparation routes were already described in our previous paper [16]. In summary, the samples are prepared in a single step, starting from inorganic nitrate precursors and using as gelling agent citric acid (the "Cit" synthesis) or polyethyleneglycol (PEG). The PEG route allows the synthesis at the same time of both the oxide components and of the Pd-containing phase. An overview of the materials investigated in this paper is provided in Table 1, giving also the key for decoding the acronyms designating the compounds, the respective molar ratios of La, Al and Ce exploited in the synthesis and the composition of the solid solution $Ce_{1-x}La_xO_{2-x/2}$. The latter parameter was determined from the XRD data, assuming a linear dependence of the lattice constant of the mixed oxide on the La content [16]. Besides these samples, the EXAFS experiments were carried out also on cerium oxide prepared by the PEG sol–gel route and on two reference compounds, CeO_2 (Aldrich, powder, $<5\,\mu m$, 99.9%) and $LaAlO_3$ (Alfa Aesar, a Johnson Matthey Company, 99.9% metals basis).

2.2. Data collection

EXAFS experiments at the Ce (40.443 keV) and La (38.920 keV) K-edges have been performed at the ESRF on the Swiss-Norwegian beamline (SNBL, BM1). The incident X-ray beam was monochromatized by a Si(111) channel-cut monochromator. The energy calibration was carried out with the CeO_2 and $LaAlO_3$ reference compounds. EXAFS measurements were performed in transmission geometry, with two krypton/nitrogen-filled ionization chambers to detect the incident (I_0) and the transmitted (I_t) beam. For each sample at least two scans were collected.

The samples have been crushed by grinding in a mortar, pressed in self-supporting wafers and mounted in an in situ EXAFS cell [33] filled with helium. The EXAFS experiments were carried out at liquid nitrogen temperature to limit the thermal disorder effects which damp the EXAFS oscillations.

The edge jumps in total absorption were greater than 0.7 for all the samples, allowing to get a good signal-to-noise ratio. The absorption jumps calculated on the basis of the samples nominal composition were in good agreement (to within a few percent) with the

Table 1
Investigated samples and nominal La:Ce, Al:Ce, La:Al, Pd:Ce molar ratios. The $x/1-x$ values in the $Ce_{1-x}La_xO_{2-x/2}$ solid solutions, calculated by XRD analysis, are reported

Sample[a]	La:Ce	Al:Ce	La:Al	Pd:Ce	$x/1-x$[b]
CeO_2	—	—	—	—	—
CeO_2–PEG	—	—	—	—	—
$LaAlO_3$	—	—	1	—	—
CLAP1	0.40	3.56	0.11	—	0.17
CLAP2	0.37	6.96	0.05	—	0.14
CLAP3	0.40	17.5	0.02	—	0.04
CLAP4	0.38	24.2	0.01		0.05
CLAC1	0.39	3.58	0.11	—	0.08
CLP1	0.25	—	—	—	0.20
					0.33
PdCLAP	0.42	4.29	0.10	0.06	0.15
CLAP5	0.39	3.53	0.11	—	0.19

[a] C, cerium; L, lanthanum; A, aluminum; P, PEG synthesis route; the second C, Cit synthesis route.
[b] La:Ce ratio in the $Ce_{1-x}La_xO_{2-x/2}$ solid solution, determined by XRD.

experimental values, so ensuring that the syntheses were carried out without loss of reagents.

2.3. Data analysis

Data extraction and EXAFS analysis were carried out by the GNXAS package [34,35]. This procedure allows to analyze raw X-ray absorption spectra without the necessity of data pre-treatments such as EXAFS extraction and Fourier filtering. The approach is based on a fitting procedure that optimizes the agreement between a model absorption signal $\alpha_{mod}(E)$ and the experimental one $\alpha_{exp}(E)$. The non-linear multiparametric fit is performed by using the CERN library subroutine MINUIT, that allows to carry out a detailed error analysis on the fitting parameters to achieve a good estimate of the confidence interval on the final results. The statistical errors on parameters are evaluated according to the size of ellipses which enclose in the parameter space χ^2 values with a confidence of 95% [36]. The model absorption is a function of the photon energy and is given by

$$\alpha_{mod}(E) = J\sigma_0(E)[1 + S_0^2\chi_{mod}(E-E_0) + \alpha_{background}(E) + \alpha_{excitation}(E)]. \quad (1)$$

The EXAFS model $\chi_{mod}(E-E_0)$ is calculated according to the multiple scattering (MS) approximation [34]. In the GNXAS analysis, the local atomic arrangement around the absorbing atom is decomposed into model atomic configurations containing $2, 3, \ldots, n$ atoms. For each configuration the atomic phase shifts are calculated using the most opportune exchange and correlation potentials in the muffin–tin approximation. The use of complex Hedin–Lundqvist potentials permits a correct inclusion of the effects due to inelastic losses. The contributions to the EXAFS signal are expressed in terms of irreducible n-body $\gamma^{(n)}$ functions which are calculated considering the effects of all the possible single and MS paths between the n-atoms. The theoretical EXAFS signal $\chi(k)$ is given by the sum of the $\gamma^{(n)}$:

$$\chi(k) = \sum_n \gamma^{(n)}, \quad (2)$$

where $k = [(2m_e/\hbar^2)(E-E_0)]^{1/2}$ is the modulus of the photoelectron wave vector.

The parameter S_0^2 in Eq. (1) is the constant reduction factor for EXAFS intensity and accounts for an effective many-body corrections to the one-electron cross-section. $\sigma_0(E)$ is an arctangent step-like function accounting for the atomic cross-section of the absorption of the atom of interest. The edge jump J accounts for the actual surface density of the photoabsorber atoms and is optimized by MINUIT. The background term $\alpha_{background}(E)$ is a smooth polynomial spline function accounting for the pre- and post-edge contribution of all absorption channels. The knots of the splines are defined in the analysis, while MINUIT optimizes the spline coefficients. The last term $\alpha_{excitation}(E)$ can take into account the possible multielectron excitation in the absorber atom adding one or more edges to the above reported equation [37].

Fig. 1a shows the edge of the reference CeO_2 and Fig. 1b the term accounting for atomic absorption. The non-monotonic atomic-XAFS determined by the spline procedure is in good agreement with literature data [38] on CeO_2 K-edge. Confirming the comparative analysis performed by Fonda et al. [22] on the Ce K- and L_{III}-edges of CeO_2, it was not necessary to take into account multielectron excitations. The edge energy E_0 was refined in a range of ± 5 eV around the maximum derivative of the absorption coefficient vs. energy data. All the spectra were analyzed by a k-weighting scheme,

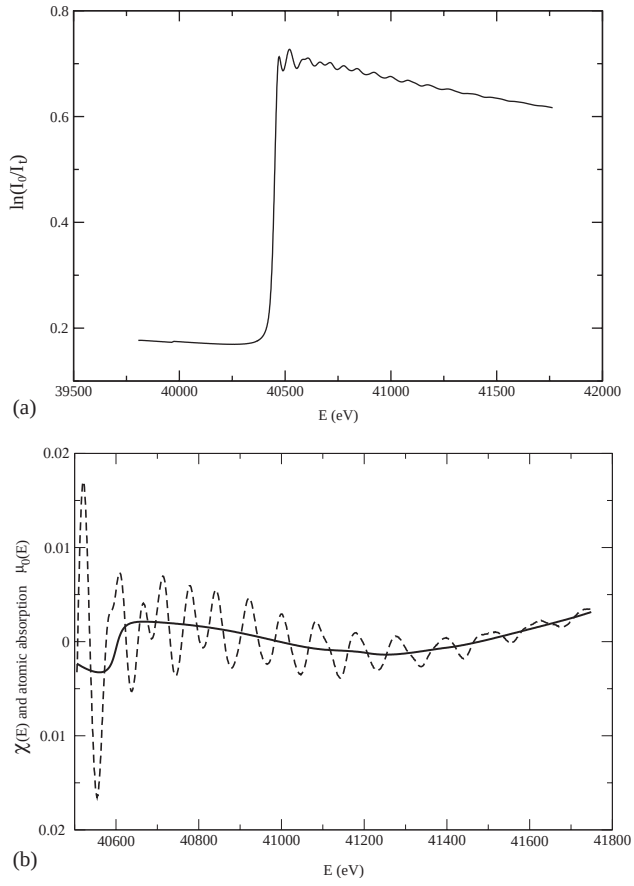

Fig. 1. (a) X-ray absorption spectrum of the reference CeO_2 compound at the Ce K-edge. (b) EXAFS oscillations (dashed line) and atomic absorption (solid line) obtained from the raw data of Fig. 1a by subtraction of the pre-edge contribution and fitting of Eq. (1).

in order to get a detailed information about the interactions of cerium and lanthanum with the light species present in the samples. The suitability of the model was evaluated also by comparison of the Fourier transform (FT) of the experimental EXAFS signal, calculated in the k-interval 3–17 $Å^{-1}$, and of the sum of the model $\gamma^{(n)}$ functions.

3. Results and discussion

All the EXAFS spectra at the Ce K-edge were analyzed with two frequency components, corresponding to the Ce–O and Ce–Ce(La) first neighbors interactions proper of the fluoritic structure, respectively. Owing to the nearly equal atomic number, Ce backscatterer could not be discriminated from La in the lanthanum-doped samples. The experimental and calculated $k\chi(k)$ functions of the reference CeO_2 compound are reported in Fig. 2a, while the respective FTs are given in Fig. 2b. Fig. 3a reports the Ce K-edge $k\chi(k)$ signals of the investigated Ce–La samples and, for

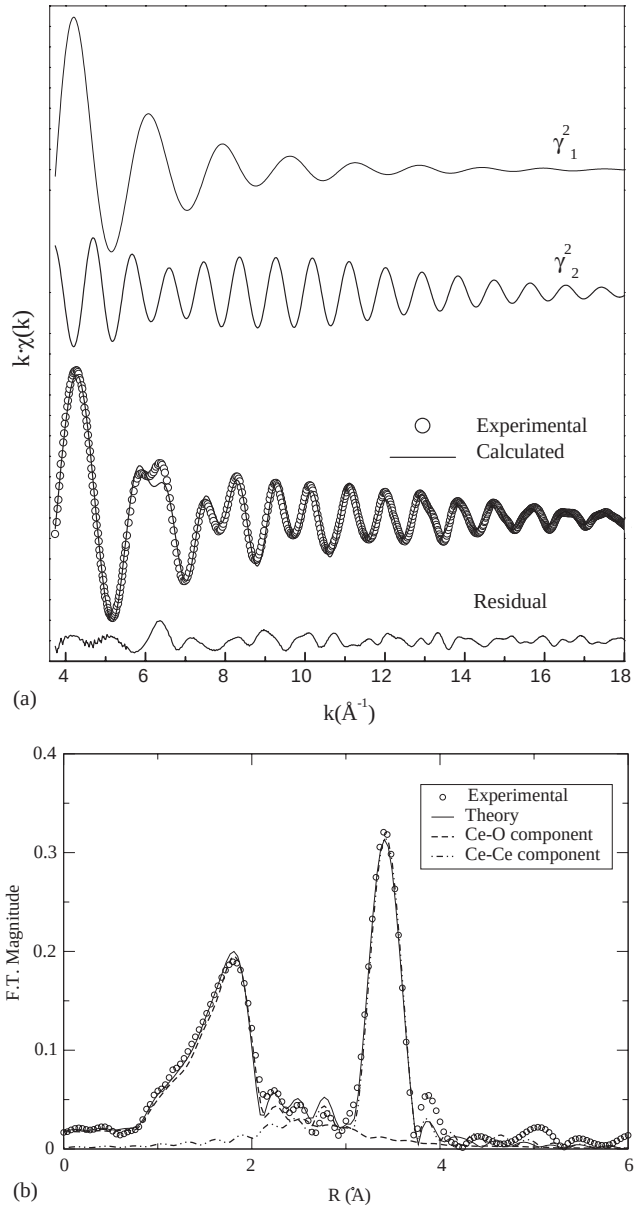

Fig. 2. (a) Experimental (circles) and fitted (solid line) $k\chi(k)$ pattern of the reference CeO_2 compound. The difference pattern is reported in the bottom part of the drawing. The two-body contributions relative to the Ce–O ($\gamma_1^{(2)}$) and, respectively, to the Ce–Ce ($\gamma_2^{(2)}$) interactions are shown in the topmost part of the figure. (b) FTs not corrected for phase shift of the experimental (circles) and calculated (solid line) $k\chi(k)$ functions. The FT of the Ce–O and Ce–Ce components are also shown.

comparison, also those of CeO_2 and CeO_2–PEG. The calculated signals are built up with the two frequency components shown in Fig. 2a, obtaining satisfactory agreement with the experimental data, as it is demonstrated also by comparison of the respective FTs shown in Fig. 3b. The attempt of introducing in the model also contributions from cerium aluminate, defined on the basis of crystallographic data [39], was discarded by MINUIT. This confirms that the formation of $CeAlO_3$

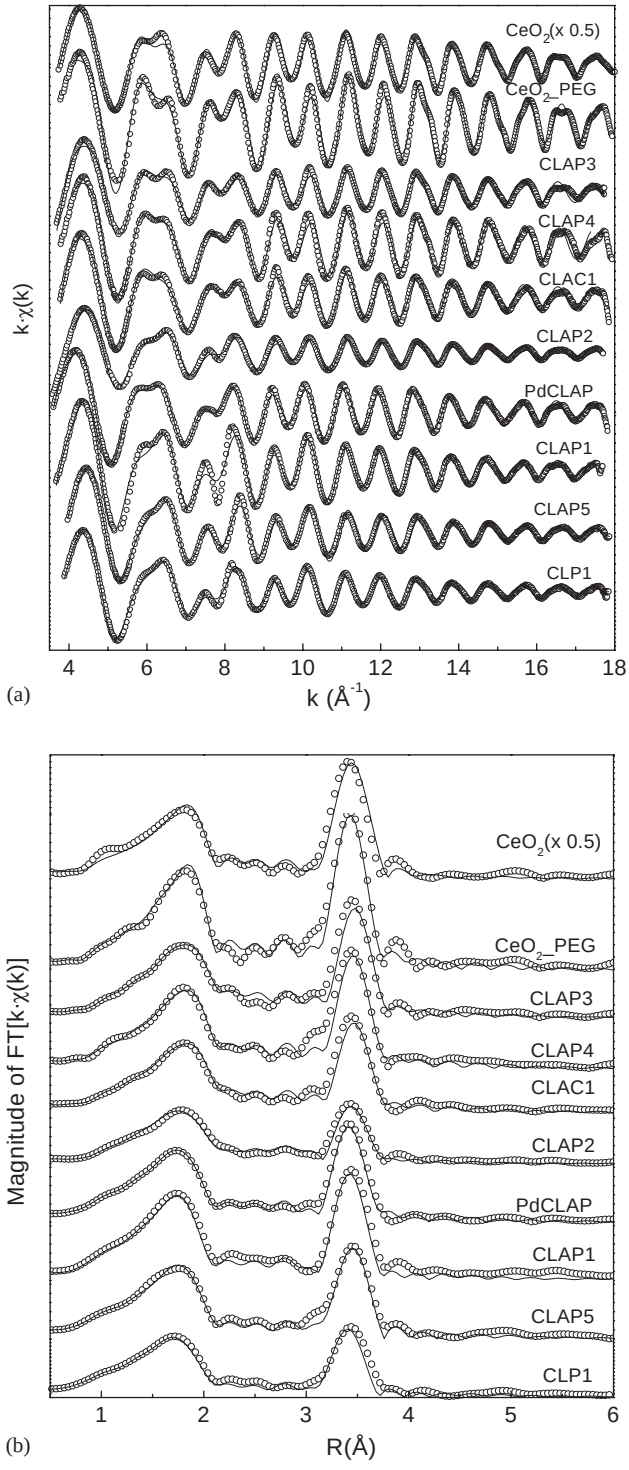

Fig. 3. (a) Experimental (circles) and fitted (solid lines) $k\chi(k)$ patterns of the investigated Ce–La samples at the Ce K-edge. For comparison, also those of CeO_2 and CeO_2–PEG are reported. The calculated patterns are generated with the two $\gamma^{(2)}$ functions reported in Fig. 1. (b) Experimental (circles) and calculated (solid lines) FTs. The FT's are uncorrected for phase shift.

is inhibited by the presence of lanthanum [40]. The reliability of this conclusion is supported, on the other hand, also by the consideration that cerium aluminate can normally be synthesized at high temperature and in reducing environment [7]. By inspection of the best-fit parameters reported in Table 2, it results that the coordination numbers of the first shell around the absorber are generally close to the value $N = 8$ proper of the fluoritic environment. On the contrary, the coordination numbers of the second Ce(La) shell are definitely smaller than the value $N = 12$ of the reference CeO_2 in all the samples synthesized by sol–gel and in particular in CeO_2–PEG. For the sol–gel samples, the Debye–Waller factors of the oxygen shell are systematically larger than those of the second shell. This behavior is not surprising, taking into account that the thermal disorder affects to a greater extent the light atoms. The coordination numbers of the first shell demonstrate that the building blocks of CeO_2–PEG and of the ceria–lanthana solid solutions are mostly constituted by eight-coordinated cerium. However, as proven by the low metal–metal coordination numbers, these building blocks form a defective tridimensional lattice. Similar results, concerning both coordination numbers and Debye–Waller factors, were found also in other EXAFS studies on oxide materials. In particular, Feth et al. [41] reported that titania–zirconia samples grown by sol–gel are constituted by edge-connected chains of $(Ti/Zr)O_6$ octahedra (with, therefore, metal–metal coordination numbers close to 1), while Lee et al. [20] demonstrated that nanocrystalline ceria have, even for very small ($\sim$2 nm) crystallite size, about eight oxygen first neighbors and only eight Ce second neighbors.

The La K-edge analysis of the reference compound $LaAlO_3$, having a distorted perovskite structure, was carried out on the basis of the distances of the crystal structure corresponding to the space group *R*-3*c* [42]. A similar compound, $LaCoO_3$, belonging to the same space group, was recently investigated at Co and La K-edges [43]. A satisfactory fitting was achieved taking into account: (i) three La–O distances at about 2.49, 2.67, and 2.98 Å that give rise in the FT to a composite La–O shell; (ii) an average La–Al distance corresponding to the two close distances in the crystalline compound at about 3.30 Å; and (iii) one La–La distance at 3.79 Å. Besides the above-quoted two-body interactions, also a three-body La–O–La term was taken into account. As the angle between the two La–O bonds is about 180°, MS becomes relevant. This contribution corresponds to a La–La distance of 5.34 Å (twice the La–O at 2.67 Å distance) and is therefore characteristic of the long-range order in crystalline $LaAlO_3$. The details of the EXAFS signal reconstruction are reported in Fig. 4a and the corresponding Fourier transforms are given in Fig. 4b.

Due to the absence of aluminum in the composition, the analysis of CLP1 required only two components corresponding to the fluorite-type La–O and La–Ce(La)

Table 2
Best fit achieved at the Ce K-edge

Sample	$x/(1-x)$	$\gamma_1^{(2)}$ Ce–O			$\gamma_2^{(2)}$ Ce–Ce(La)		
		R (Å)	N	σ^2 (Å^2)	R (Å)	N	σ^2 (Å^2)
CeO_2		2.32(1)	8	2.6(5)	3.80(2)	12	2.8(6)
CeO_2–PEG		2.31(1)	7.9(4)	3.2(6)	3.77(2)	6.5(5)	1.0(1)
CLAP3	0.04	2.32(1)	6.5(4)	6.6(5)	3.80(2)	3.7(4)	1.0(1)
CLAP4	0.05	2.32(1)	7.9(4)	4.6(5)	3.79(2)	4.6(5)	1.0(2)
CLAC1	0.08	2.33(2)	8.0(4)	5.8(5)	3.80(3)	3.8(4)	1.0(1)
CLAP2	0.14	2.29(1)	6.2(4)	7.1(5)	3.79(3)	2.8(7)	2.0(1)
PdCLAP	0.15	2.29(1)	8.0(4)	5.3(5)	3.79(2)	4.5(5)	2.0(1)
CLAP1	0.17	2.27(1)	8.0(4)	4.0(1)	3.79(3)	6.6(5)	3.0(2)
CLAP5	0.19	2.27(1)	8.0(4)	4.8(5)	3.78(2)	4.9(5)	1.9(4)
CLP1	0.24	2.26(1)	8.0(4)	6.6(4)	3.79(3)	4.0(4)	2.3(5)

The samples are ordered according to increasing La content in $Ce_{1-x}La_xO_{2-x/2}$.

distances. The respective $\gamma^{(2)}$ functions are shown in Fig. 5, showing also the comparison between the resulting calculated pattern and the experimental EXAFS spectrum.

In principle, the aluminum-bearing samples could be characterized by the simultaneous presence of both the perovskite- and fluorite-type contributions shown in Figs. 4 and 5. In Fig. 6a the experimental EXAFS signals (circles) are reported for all the investigated samples at the La K-edge. Sample CLAP3 is reported as well, although the pattern could be recorded only to about 14 Å. The corresponding FTs in Fig. 6b present the MS La–O–La shell for those samples (CLAP5, PdCLAP, CLAP1, and CLAP2) having also a recognizable $LaAlO_3$ contribution in the XRD pattern [16]. The presence of the perovskite phase in these samples finds a further evidence in the La–Al shell midway between the La–O and the La–Ce(La) ones. The fluorite-type La–O and La–Ce(La) distances are very similar to the La–O at 2.49 Å and, respectively, to the La–La distance at 3.79 Å in $LaAlO_3$. So, the analysis of the EXAFS La K-edge signals were carried out with: (i) two La–O distances (that could be attributed to the fluorite-type at ~2.46 Å and, respectively, to the average perovskite-type La–O at ~2.67 Å); (ii) one La–Al perovskite-type distance at about 3.3 Å; (iii) one La–Ce(La) frequency component accounting simultaneously for the perovskite- and fluorite-type contributions; and (iv) the La–O–La MS perovskite-like term. The samples CLP1, CLAC1, CLAP3, and CLAP4, not showing in the respective experimental FTs (see Fig. 6b) the peaks characteristic of the perovskite phase, were analyzed on the basis of the two fluorite-like components La–O and La–Ce(La). The complete fitting results on the La K-edge are reported in Table 3, while the solid lines in Fig. 6a and b report, respectively, the calculated EXAFS signals and the corresponding FTs.

Clearly, with the approximations used to model the EXAFS signals of the samples CLAP5, PdCLAP, CLAP1, and CLAP2, the coordination numbers reported in Table 3 represent merely an overall weight of the respective composite shells; the σ values, generally large and without a well-defined behavior through the different shell, are probably influenced by the structural disorder about lanthanum and by the spread of distances of the composite shells. From inspection of Fig. 6b, the perovskite characteristic peaks are more evident in PdCLAP; according to the results reported in Table 3, the smaller σ values point to a more ordered perovskite phase, although it is not possible to say, on the basis of the available data, if palladium has a specific role in determining this behavior. Some clue about the inclusion of La in alumina can be achieved from CLAP3 and CLAP4. In fact, these materials, characterized by the largest molar ratio between aluminum and heavy metals (see Table 1), present not only a quite small ratio between the La–Ce(La) and La–O peaks in the FT, but also small La–O coordination numbers. Therefore, it is likely that a noteworthy fraction of La is also present in the alumina matrix, with a distorted environment of oxygens. This situation probably holds for all the samples, although it is not so evident as in CLAP3 and CLAP4, due to larger La:Al ratios (see Table 1). A possible interpretation of these results is that lanthanum can be hosted in the ceria network as a dopant, or interact with aluminum to form a mixed oxide; when the La:Al molar ratio is sufficiently high, the perovskite $LaAlO_3$ network can grow. From the comparison of the respective FTs and taking into account the very similar composition reported in Table 1, the EXAFS analysis relative to CLAC1 and CLAP1 allows to conclude, in agreement with the XRD results, that the citrate method is likely to favor the dispersion of lanthanum in the alumina matrix.

Among the three phases present in the investigated three-way catalysts, the OSC is effectively provided by the $Ce_{1-x}La_x0_{2-x/2}$ solid solution. In Fig. 7a and b the Ce–O and La–O distances are reported, respectively, as

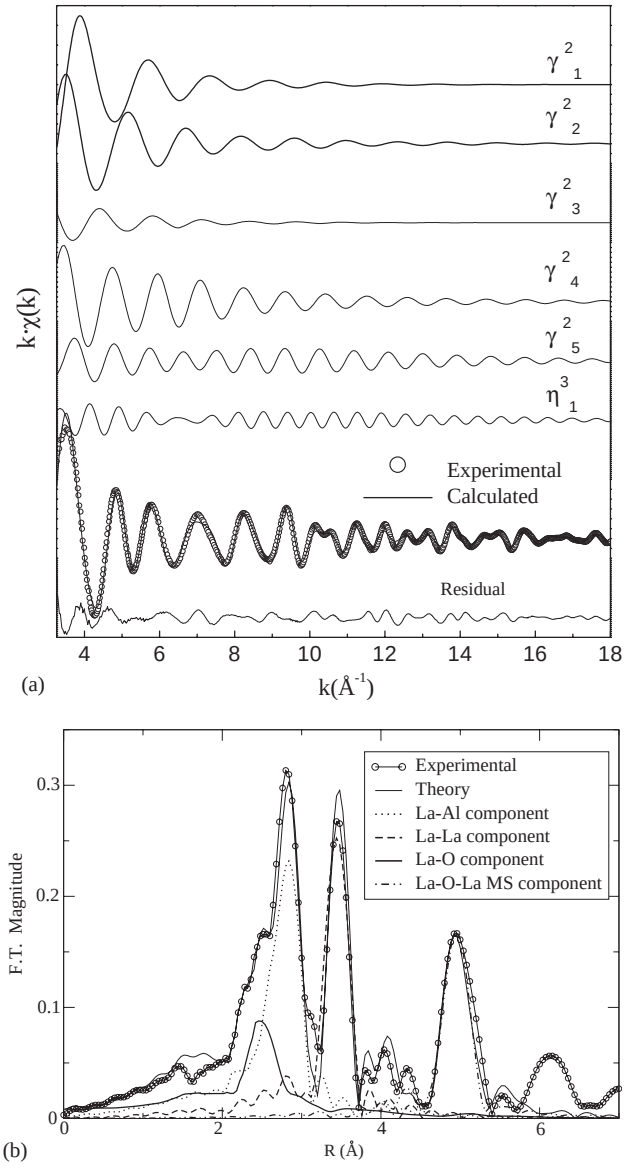

Fig. 4. (a) Experimental (circles) and fitted (solid line) EXAFS signal for the reference $LaAlO_3$ compound. The difference pattern is reported in the bottom part of the drawing. The two-body contributions relative to La–OI ($\gamma_1^{(2)}$), La–OII ($\gamma_2^{(2)}$), La–OIII ($\gamma_3^{(2)}$), La–Al ($\gamma_4^{(2)}$)) and, respectively, to the La–La ($\gamma_5^{(2)}$) interactions are shown in the topmost part of the figure. The three-body term η_1^3 relative to the MSLa–O–La paths at about 180° is also shown. (b) FT, not corrected for phase shift, of the $k\chi(k)$ functions of Fig. 4a. The three La–O signals are summed up and the resulting composite La–O shell is drawn.

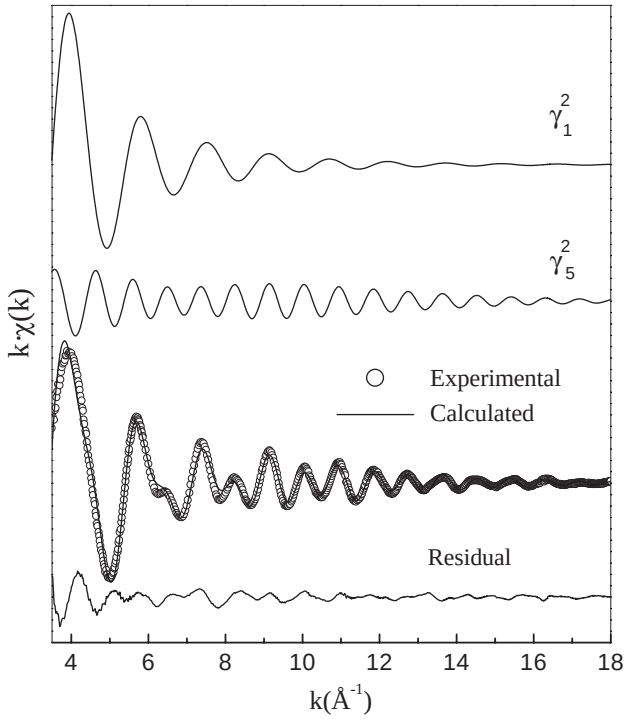

Fig. 5. Experimental (circles), fitted (solid line), and difference $k\chi(k)$ pattern for CLP1. The two-body contributions relative to the Ce–O ($\gamma_1^{(2)}$) and, respectively, to the Ce–Ce(La) ($\gamma_2^{(2)}$) interactions are shown in the topmost part of the figure.

a function of $x/1-x$ in the $Ce_{1-x}La_x0_{2-x/2}$ solid solution. From inspection of Fig. 7a, it is possible to observe that for very small $x/1-x$ values the Ce–O distance is almost constant and decreases for increasing La content. The La–O distance, Fig. 7b, seems to be nearly constant, although the uncertainty in the determination of this parameter is larger. The Ce–O contraction was already found by EXAFS experiments on ceria doped with Y, Yb, Gd, Sm, Nd [21,44], but it is the first time that exhaustive experimental data concerning the Ce–O distance are given for the ceria–lanthana mixed oxide. The metal–oxygen distances shown in Fig. 7a and b and the nearly constant metal–metal fluorite-type distances reported in Tables 2 and 3 confirm the results of molecular dynamics (MD) calculation [45] on ceria–lanthana at different dopant concentration. There is agreement also between the MD simulation, forecasting that the oxygen diffusion coefficient attains a maximum in correspondence to an optimal dopant content, and the data reported in our previous paper [16], accounting for a maximum of OSC in correspondence of $x/1-x=0.18$; interestingly, also the anionic conductivity of ceria–lanthana [46] gets to a maximum in correspondence of the same La content ($x/1-x=0.18$). This agreement is by no means surprising, as both OSC and anionic conductivity are strictly dependent on oxygen diffusivity in ceria–lanthana network.

4. Conclusion

Two sol–gel routes leading to the formation of three-way ceria–lanthana–alumina catalysts in a single preparation step have been studied by EXAFS spectroscopy. In the presence of cerium and aluminum, La is involved in the formation of a fluorite-like

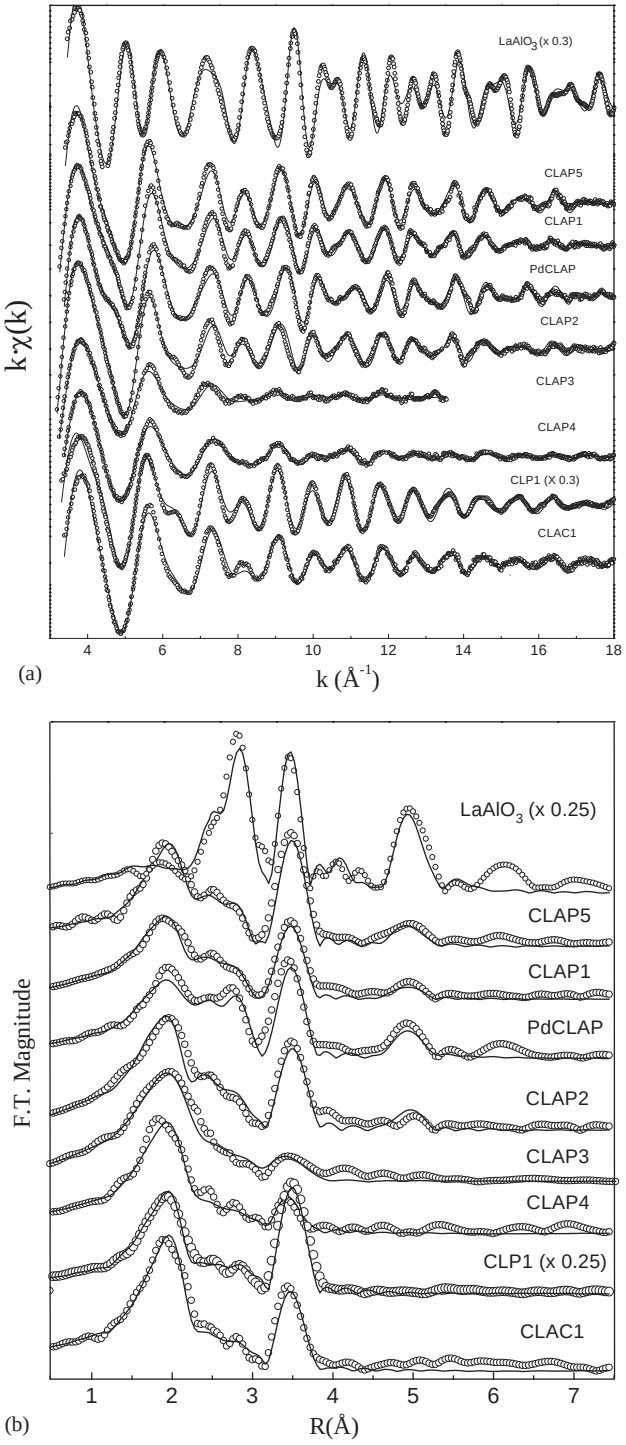

Fig. 6. (a) Experimental (circles) and calculated (solid line) $k\chi(k)$ signals for all the investigated samples at the La K-edge. (b) Experimental (circles) and calculated (solid lines) FT, not corrected for phase shift.

$Ce_{1-x}La_xO_{2-x/2}$ solid solution and of the perovskite-like $LaAlO_3$ compound, suggesting a competition between the two different environments in hosting lanthanum. Moreover, the EXAFS analysis allowed us to get an indication that La is hosted also in the alumina phase,

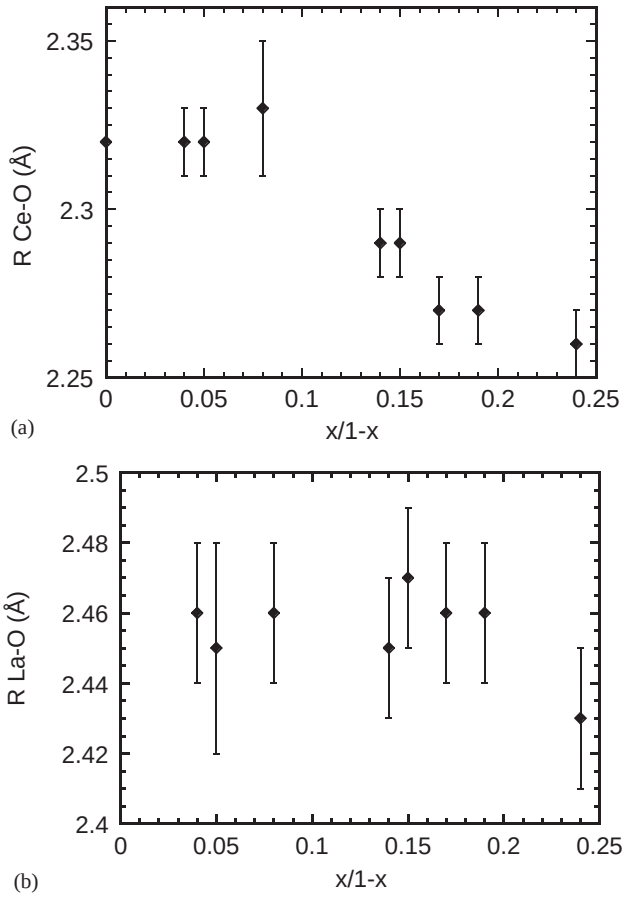

Fig. 7. Ce–O distance (Fig. 7a) and La–O distance (Fig. 7b) as a function of the La/Ce molar ratio in the $Ce_{1-x}La_x0_{2-x/2}$ solid solution. The error bars, as determined by the MINUIT error analysis, are also drawn.

supporting the hypothesis that it plays an important role in the thermal stabilization of γ-alumina. No experimental evidence of perovskite-type $CeAlO_3$ distances was observed, thus confirming the hypothesis that the formation of a cerium aluminate phase is unlikely under the exploited reaction conditions. The EXAFS analysis allowed in particular to obtain structural data concerning the $Ce_{1-x}La_xO_{2-x/2}$ phase, that is relevant for OSC. Cerium in ceria–lanthana prepared by sol–gel has a nearly complete ($N \sim 8$) first shell of oxygen atoms, but reduced second shell coordination numbers. This behavior is similar to that recognized in titania–zirconia mixed oxides prepared by sol–gel [41], characterized by regular coordination around the metal, but having a highly defective metal–metal correlation. The results of the EXAFS analysis confirm the MD calculations of Hayashi et al. [45] as it concerns the dependence of metal–oxygen and of metal–metal distances on the dopant content in $Ce_{1-x}La_xO_{2-x/2}$. This agreement extends also to the similar dependence on La concentration between the theoretical forecast of MD on oxygen diffusion coefficient and the measured OSC of the investigated materials [16].

Table 3
Best-fit parameters at the La K-edge

Sample	La:Al	$\gamma_1^{(2)}$ La–OI			$\gamma_2^{(2)}$ La–OII			$\gamma_3^{(2)}$ La–OIII			$\gamma_4^{(2)}$ La–Al			$\gamma_5^{(2)}$ La–Ce(La)			$\eta_1^{(3)}$ La–O–La (Ce)		
		R (Å)	N	σ^2 (Å^2)	R (Å)	N	σ^2 (Å^2)	R (Å)	N	σ^2 (Å^2)	R (Å)	N	σ^2 (Å^2)	R (Å)	N	σ^2 (Å^2)	θ (°)	N	σ^2 (Å^2)
$LaAlO_3$	0.5	2.49(1)	3	5.3(2)	2.67(2)	6	1.7(4)	2.98(2)	3	5.6(4)	3.30(2)	8	0.53(5)	3.79(2)	6	2.3(4)	181(1)	12	4.3(2)
CLAP5	0.11	2.46(2)	6.5(6)	5.5(2)	2.66(2)	0.8(1)	0.9(1)				3.30(3)	1.8(5)	2.5(8)	3.83(3)	3.6(5)	2.6(8)	180(1)	0.8(6)	1.9(4)
CLAP1	0.11	2.46(2)	4.8(9)	6.6(7)	2.67(2)	0.5(4)	1.4(1)				3.31(3)	1.9(7)	4.3(5)	3.85(2)	2.9(7)	3.82(7)	180(2)	0.5(7)	2.7(2)
PdCLAP	0.1	2.47(2)	4.0(7)	9.84(5)	2.66(2)	0.4(5)	0.5(1)				3.29(2)	1.7(7)	0.82(6)	3.83(3)	1.8(7)	2.8(3)	178(2)	0.4(5)	0.95(2)
CLAP2	0.05	2.45(2)	7.9(5)	3.5(7)	2.68(2)	0.6(5)	1.7(4)				3.35(3)	1.7(7)	10.5(8)	3.85(2)	2.0(7)	3.54(7)	180.01(2)	0.6(5)	1.7(9)
CLAP3	0.02	2.46(2)	3.5(7)	10.2(7)										3.84(3)	1.2(9)	9.32(9)			
CLAP4	0.01	2.45(3)	2.8(6)	6.04(7)										3.84(3)	1.0(9)	2.91(9)			
CLP1	0	2.43(2)	7.9(5)	3.5(7)										3.85(3)	7.2(8)	3.3(7)			
CLAC1	0.11	2.46(2)	3.8(7)	4.2(9)										3.85(3)	3.4(7)	3.2(8)			

The samples, with the exception of CLAC1 (see text), are ordered according to decreasing La:Al ratio.

Acknowledgments

This study was performed with the financial support of the MURST project MM03267484_002. The authors thank the scientific staff of the Swiss-Norvegian beamline BM1 of ESRF for the assistance in the EXAFS measurements and Prof. R. Prins of ETH Zurich for valuable discussion and suggestions. Finally, we acknowledge the authors of GNXAS software for user license.

References

[1] A. Trovarelli, Catal. Rev. Sci. Eng. 38 (1996) 439–519.
[2] A. Trovarelli, C. de Leitenburg, M. Boaro, G. Dolcetti, Catal. Today 50 (1999) 353–367.
[3] R.K. Usmen, G.W. Graham, W.L.H. Watkins, R.W. McCabe, Catal. Lett. 30 (1995) 53–63.
[4] T. Miki, T. Ogawa, M. Haneda, N. Kakuta, A. Ueno, S. Tateishi, S. Matsuura, M. Sato, J. Phys. Chem. 94 (1990) 6464–6467.
[5] L.F. Liotta, G. Deganello, D. Sannino, M.CG audino, P. Ciambelli, S. Gialanella, Appl. Catal. A 229 (2002) 217–227.
[6] S. Rossignol, C. Kappenstein, Int. J. Inorg. Mater. 3 (2001) 51–58.
[7] A. Piras, A. Trovarelli, G. Dolcetti, Appl. Catal. B 28 (2000) L77–L81.
[8] X. Chen, Y. Liu, G. Niu, Y. Zhuxian, B. Maiying, H. Adi, Appl. Catal. A 205 (2001) 159–172.
[9] S. Braun, L.G. Appel, L.B. Zinner, M. Schmal, Br. Ceram. Trans. 98 (1999) 77–80.
[10] N.E. Bogdanchikova, S. Fuentes, M. Avalos-Borja, M.H. Farías, A. Boronin, G. Díaz, Appl. Catal. B 17 (1998) 221–231.
[11] H. Arai, M. Machida, Appl. Catal. A 138 (1996) 161–176.
[12] K.J.D. MacKenzie, M. Schmucker, L. Mayer, Thermochim. Acta 335 (1999) 73–78.
[13] A. Galtayries, G. Blanco, G.A. Cifredo, D. Finol, J.M. Gatica, J.M. Pintado, H. Vidal, R. Sporken, S. Bernal, Surf. Interf. Anal. 27 (1999) 941–949.
[14] US Björkert, R. Mayappan, D. Holland, M.H. Lewis, J. Eur. Ceram. Soc. 19 (1999) 1847–1857.
[15] A. Vasquez, T. Lopez, R. Gomez, X. Bokhimi, J. Mol. Catal. A 167 (2001) 91–99.
[16] F. Deganello, A. Martorana, J. Solid State Chem. 163 (2002) 527–533.
[17] J.H. Holles, R.J. Davis, J. Phys. Chem. 104 (2000) 9653–9660.
[18] E. Fonda, D. Andreatta, P.E. Colavita, G. Vlaic, J. Synchrotron Radiat. 6 (1999) 34–42.
[19] P. Nachimuthu, W.-C. Shih, R.-S. Liu, L.-Y. Jang, J.-M. Chen, J. Solid State Chem. 149 (2000) 408.
[20] J.-F. Lee, M.-T. Tang, W.C. Shih, R.S. Liu, Mater. Res. Bull. 37 (2002) 555–562.
[21] S. Yamazaki, T. Matsui, T. Ohashi, Y. Arita, Solid State Ionics 136–137 (2000) 913–920.
[22] H. Yoshida, H. Deguchi, K. Miura, M. Horiuchi, T. Inagaki, Solid State Ionics 140 (2001) 191–199.
[23] G. Vlaic, P. Fornasiero, S. Geremia, J. Kaspar, M. Graziani, J. Catal. 168 (1997) 386–392.
[24] S. Lemaux, A. Bensaddik, A.M.J. van der Eerden, J.H. Bitter, D.C. Koningsberger, J. Phys. Chem. B 105 (2001) 4810–4815.
[25] J. Hormes, M. Pantelouris, G.B. Balazs, B. Rambabu, Solid State Ionics 136–137 (2000) 945–954.
[26] F. Ali, A.V. Chadwick, M.E. Schmitz, J. Mater. Chem. 7 (1997) 285–291.
[27] Y. Nagai, T. Yamamoto, T. Tanaka, S. Yoshida, T. Nonaka, T. Okamoto, A. Suda, M. Sugiura, Catal. Today 74 (2002) 225–234.
[28] A. Vasquez, T. Lopez, R. Gomez, X. Bokhimi, A. Morales, O. Novaro, J. Solid State Chem. 128 (1997) 161–168.
[29] M. Ozawa, M. Kimura, A. Isogai, J. Less-Common Met. 162 (1990) 297–308.
[30] L.P. Haack, J.E. de Vries, K. Otto, M.S. Chattha, Appl. Catal. A 82 (1992) 199–214.
[31] L.J. Alvarez, J.P. Jacobs, J.F. Sanz, J.A. Odriozola, Solid State Ionics 95 (1997) 73–79.
[32] M.J. Capitan, M.A. Centeno, P. Malet, I. Carrizosa, J.A. Odriozola, A. Marquez, J. Fernandez Sanz, J. Phys. Chem. 99 (1995) 4655–4660.
[33] F.W.H. Kampers, T.M.J. Maas, J. van Grondelle, P. Brinkgreve, D.C. Koningsberger, Rev. Sci. Instrum. 60 (1989) 2635–2638.
[34] A. Filipponi, A. Di Cicco, C.R. Natoli, Phys. Rev. B 52 (1995) 15122–15134.
[35] A. Filipponi, A. Di Cicco, Phys. Rev. B 52 (1995) 15135–15149.
[36] F. James, MINUIT Function Minimization and Error Analysis, CERN Program Library Long Writeup D506, CERN Geneva, Switzerland, 1994.
[37] A. Filipponi, A. Di Cicco, Phys. Rev. A 52 (1995) 1072–1078.
[38] J.J. Rehr, S.I. Zabinski, A. Ankudinov, R.C. Albers, Physica B 208–209 (1995) 23–26.

[39] M. Tanaka, T. Shishido, H. Horiuki, N. Toyota, D. Shindo, T. Fukuda, J. Alloys Compounds 192 (1993) 87–89.
[40] G.W. Graham, P.J. Schmitz, R.K. Usmen, R.W. McCabe, Catal. Lett. 17 (1993) 175–184.
[41] M.P. Feth, A. Weber, R. Merkle, U. Reinhöl, H. Bertagnolli, J. Non-Cryst. Solids 298 (2002) 43–52.
[42] D.J. du Boulay, Structure, vibration and electron density in neodymium–iron-boride and some rare-earth perovskite oxides, Ph.D. Thesis, University of Western Australia, February 1996 (Chapter 6).
[43] S. Colonna, S. De Rossi, M. Faticanti, I. Pettiti, P. Porta, J. Mol. Catal. A 180 (2002) 161–168.
[44] T. Ohashi, S. Yamazaki, T. Tokunaga, Y. Arita, T. Matsui, T. Harami, K. Kobayashi, Solid State Ionics 113–115 (1998) 559–564.
[45] H. Hayashi, R. Sagawa, H. Inaba, K. Kawamura, Solid State Ionics 131 (2000) 281–290.
[46] S. Dikmen, P. Shuk, M. Greenblatt, Solid State Ionics 126 (1999) 89–95.